

# Kinetic simulations of compressible non-ideal fluids: from supercritical to phase-change and exotic behavior

Ehsan Reyhanian, Benedikt Dorschner and Ilya Karlin\*

Department of Mechanical and Process Engineering, ETH Zurich, 8092 Zurich, Switzerland

\* Correspondence: [ikarlin@ethz.ch](mailto:ikarlin@ethz.ch)

Received: date; Accepted: date; Published: date

**Abstract:** In this study, we present a thorough investigation of a compressible kinetic model for non-ideal fluids [DOI:10.1103/PhysRevE.102.020103]. The model imposes the local thermodynamic pressure through appropriate rescaling of the particle's velocities, which accounts for both long- and short-range effects and hence full thermodynamic consistency. The model is fully Galilean invariant and treats mass, momentum, and energy as local conservation laws. After detailed analysis and derivation of the hydrodynamic limit, the model's accuracy and robustness is assessed for various benchmark simulations ranging from Joule-Thompson effect, phase-change and high-speed flows. We show that our model can operate in the entire phase diagram, including super- as well as sub-critical regimes and inherently captures phase-change phenomena.

**Keywords:** non-ideal fluids, kinetic theory, lattice Boltzmann method

---

## 1. Introduction

The lattice Boltzmann method (LBM) is a kinetic-based approach for the simulation of hydrodynamic phenomena with applications ranging from turbulence [1,2] to micro [3,4] and multiphase flows [5–8]. The fully discretized kinetic equations evolve particle distribution functions (populations)  $f_i(x, t)$ , associated with a set of discrete velocities  $c_i$ , according to a simple stream-and-collide algorithm, which recovers the Navier-Stokes equations in the hydrodynamic limit [9].

Despite significant success of the LBM in isothermal incompressible flow applications [10–13], the simulation of compressible flows with the LBM is still an active field of research. Furthermore, the majority of studies concern ideal gases, which is inherent to the LBM. However, the ideal-gas assumption is no longer valid in many scientific and engineering applications and real-gas effects have to be taken into account. This includes phenomena such as rarefaction shock waves [14–17], the acoustic emission instability [18,19], inversion line (change of sign of the Joule-Thomson coefficient), phase transition, surface tension and super-critical flows. Hence, developing a compressible scheme with a non-ideal equation of state (EOS) remains an uncharted territory within the LBM and is subject to this paper.

For incompressible flows, two main approaches have been proposed so far to model non-ideal gas flows within the LBM context: pressure-based methods [20,21] and forcing methods [22–25]. In pressure-based methods, the equilibrium populations are altered directly and constructed such that the full non-ideal pressure tensor, including the non-ideal EOS and the Korteweg stress, are recovered. However, as shown in [26] these methods lack thermodynamic consistency. On the other hand, forcing methods account for the deviation from the ideal-gas pressure by an appropriate (non-local) force term, which is introduced in the kinetic equations. Promising results have been obtained for various of applications, ranging from droplet collisions at relatively large density ratios [27,28] to droplet impact on textured [29] and flexible surfaces [30]. Furthermore, these methods have been extended to thermal multiphase flows including phase-change [31,32]. Note however that these models are still assuming incompressible flow

and thus do not recover the correct energy equation of the two-phase system. The temperature field is then typically modeled as a passive scalar field under various assumptions, which leads to a tailored form of the energy equation with additional correction terms to account for the latent heat [33].

To mitigate these shortcomings, we recently proposed a novel method for non-ideal compressible fluid dynamics [34] based on adaptive discrete velocities in accordance to local flow conditions. In contrast to the aforementioned schemes, the model features full Galilean-invariance and is thermodynamically consistent. As a consequence, the full energy-equation of a non-ideal fluid is recovered, which means that no additional phase-change model is required. This enables us to capture a large range of flow regimes, which we aim to explore in this paper. In particular, we will assess the model's performance and range of validity for benchmarks ranging from super-critical flows, throttling, phase change to shock-stability.

The paper is structured as follows: Section 2 provides an in-depth analysis of the model, starting by a presentation of the discrete kinetic equations in Sec. 2.1. Finally, the Chapman-Enskog analysis and the derivation of the hydrodynamic limit of the model is carried out in Sec. 2.2. Numerical benchmarks including the simulation of the Joule-Thomson effect, phase-change and high-speed flows are presented in Sec. 3. Finally, conclusions are drawn in Sec. 4.

## 2. Methodology

### 2.1. Kinetic equations

Our thermokinetic model of non-ideal fluids [34] is based on the so-called Particles-on-Demand (PonD) method [35], which constructs the particle's velocities relative to the reference frame (gauge)  $\lambda = \{T, \mathbf{u}\}$ , where  $T$  is the local temperature and  $\mathbf{u}$  is the local velocity. While the former leads to thermodynamic consistency, the latter guarantees Galilean invariance. In addition, in the local reference frame, the local equilibrium becomes exact and solely dependent on the density. This is in contrast to classical LBM where one typically resorts to a truncated polynomial. The populations can be transformed between different reference frames by requiring the moments to be independent of the reference frame [35]. In [34], we generalized this concept to encompass the thermodynamics of non-ideal fluids by defining the new set of discrete velocities as

$$\mathbf{v}_i = \sqrt{\frac{p}{\rho T_L}} \mathbf{c}_i + \mathbf{u}, \quad (1)$$

where  $p(\mathbf{x}, t)$  is the local thermodynamic pressure,  $\rho(\mathbf{x}, t)$  is the local density and  $T_L$  is a lattice reference temperature, a constant known for any set of speeds  $\mathcal{C} = \{\mathbf{c}_i, i = 1, \dots, Q\}$ , and  $\mathbf{u}(\mathbf{x}, t)$  is the local flow velocity.

A two-population approach has been employed in this study. While  $f$  populations maintain the density and the momentum field, the  $g$  populations carry the total-energy. As in classical LBM, a simple stream and collide algorithm is used to evolve the populations in time. In particular, we use a semi-Lagrangian approach for advection along the characteristics [36,37] at the monitoring point  $(\mathbf{x}, t)$ , which reads

$$f_i^\lambda(\mathbf{x}, t) = \tilde{f}_i^\lambda(\mathbf{x} - \mathbf{v}_i \delta t, t - \delta t), \quad (2)$$

$$g_i^\lambda(\mathbf{x}, t) = \tilde{g}_i^\lambda(\mathbf{x} - \mathbf{v}_i \delta t, t - \delta t), \quad (3)$$

while the Bhatnagar-Gross-Krook (BGK) model is employed for the collision step

$$f_i(\mathbf{x}, t) = f_i^\lambda(\mathbf{x}, t) + \omega(f_i^{\text{eq}} - f_i^\lambda(\mathbf{x}, t)) + S_i^\lambda, \quad (4)$$

$$g_i(\mathbf{x}, t) = g_i^\lambda(\mathbf{x}, t) + \omega(g_i^{\text{eq}} - g_i^\lambda(\mathbf{x}, t)) + G_i^\lambda \delta t, \quad (5)$$

where  $\{f_i^{eq}, g_i^{eq}\}$  denote the equilibrium populations. The source terms  $\{S_i^\lambda, G_i^\lambda\}$  are used to account for the effect of surface tension in the momentum equation and a correction term in the energy equation, respectively. Details will be provided in sections 2.1.3 and 2.1.2.

It is important to note that since the discrete velocities (1) depend on the local flow field (pressure, density and velocity), the departure point  $x_d = x - v_i \delta t$  does not necessarily coincide with a grid node. Thus, the populations at the departure point need to be reconstructed and we use the general interpolation scheme

$$\{\tilde{f}^\lambda(x_d, t), \tilde{g}^\lambda(x_d, t)\} = \sum_{p=0}^N \Lambda(x_d - x_p) \mathcal{G}_{\lambda_p}^\lambda \{f^{\lambda_p}(x_p, t), g^{\lambda_p}(x_p, t)\}, \quad (6)$$

where  $x_p, p = 0, \dots, N$  denote the collocation points (grid points) and  $\Lambda$  is the interpolation kernel. Notice that the population at the collocation points are, in general, not in the same reference frame as the populations at the monitoring points. Thus, during the reconstruction step populations are transformed from the reference from  $\lambda_p$  to  $\lambda$  through the transformation matrix  $\mathcal{G}_{\lambda_p}^\lambda$  [35]. In general, a set of populations at gauge  $\lambda$  can be transformed to another gauge  $\lambda'$  by matching  $Q$  linearly independent moments

$$\mathbf{M}_{mn}^\lambda = \sum_{i=1}^Q f_i^\lambda v_{ix}^m v_{iy}^n, \quad (7)$$

where  $m$  and  $n$  are integers. This may be written in the matrix product form as  $\mathbf{M}^\lambda = \mathcal{M}_\lambda f^\lambda$  where  $\mathcal{M}$  is the  $Q \times Q$  linear map. Finally, requiring that the moments must be independent from the choice of the reference frame, leads to the matching condition

$$\mathcal{M}_{\lambda'} f^{\lambda'} = \mathcal{M}_\lambda f^\lambda, \quad (8)$$

which leads to the transformed populations

$$f^{\lambda'} = \mathcal{G}_{\lambda'}^{\lambda'} f^\lambda = \mathcal{M}_{\lambda'}^{-1} \mathcal{M}_\lambda f^\lambda. \quad (9)$$

Finally, we comment that the choice of the interpolation kernel is not the focus of the current study and will be addressed in our future publications. For simplicity, we use the third-order Lagrange polynomials in what follows, unless stated otherwise.

With the transformations defined, we are set for the advection scheme, where the local gauge is found iteratively using a predictor-corrector scheme. The full algorithm is depicted in Fig. 1. Initially, the discrete velocities (1) are defined relative to the gauge  $\lambda_0 = \{p_0/\rho_0, \mathbf{u}_0\}$  based on the pressure, density and velocity field from the previous time step. Once the discrete velocities  $v_i^0$  are set, the semi-Lagrangian advections (2) and (3) are performed. With the new populations at the monitoring point, the density, momentum and total energy are evaluated by taking the corresponding moments of each population,

$$\rho_1 = \sum_{i=1}^Q f_i^{\lambda_0}, \quad (10)$$

$$\rho_1 u_{\alpha_1} = \sum_{i=1}^Q f_i^{\lambda_0} v_{i\alpha}^0, \quad (11)$$

$$2\rho_1 e_1 + \rho_1 u_1^2 = \sum_{i=1}^Q g_i^{\lambda_0}, \quad (12)$$

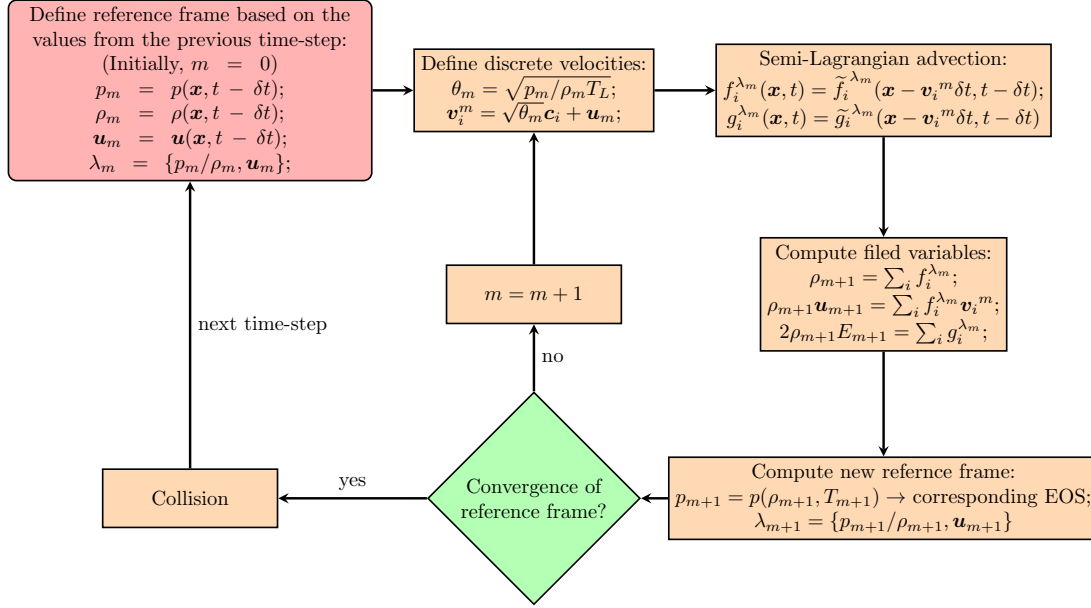


**Figure 1.** Flowchart of the semi-Lagrangian advection using the predictor-corrector algorithm.

where  $e = e(\rho, T)$  is the internal energy of a non-ideal fluid. Subsequently, the pressure can be evaluated using the EOS of choice using the updated values for density and temperature. Finally, we can define the corrector gauge as  $\lambda_1 = \{p_1/\rho_1, \mathbf{u}_1\}$  with  $v_i^1 = \sqrt{p_1/(\rho_1 T_L)} c_i + \mathbf{u}_1$ . This predictor-corrector step is iterated until the convergence of the gauge is achieved, where the limit gauge is the co-moving reference frame. Once the co-moving reference frame is determined, the advectations (2) and (3) are completed. Finally, the collision step in the co-moving reference frame follows. For the  $f$  populations the local equilibrium takes the exact form

$$f_i^{\text{eq}} = \rho W_i, \quad (13)$$

where  $W_i$  are lattice weights, which are known for any velocity set. The equilibrium for the  $g$  population is derived using Grad's approximation [38–40] for the new discrete velocities (1). Thus, the equilibrium populations are constructed from the moments

$$M^{\text{eq}} = \sum_{i=0}^Q g_i^{\text{eq}}, \quad q_\alpha^{\text{eq}} = \sum_{i=0}^Q g_i^{\text{eq}} v_{i\alpha}, \quad R_{\alpha\beta}^{\text{eq}} = \sum_{i=0}^Q g_i^{\text{eq}} v_{i\alpha} v_{i\beta}, \quad (14)$$

where the explicit relations for the equilibrium moments are given by

$$M^{\text{eq}} = 2\rho E, \quad (15)$$

$$q_\alpha^{\text{eq}} = 2\rho u_\alpha H, \quad (16)$$

$$R_{\alpha\beta}^{\text{eq}} = 2\rho u_\alpha u_\beta (H + p/\rho) + 2pH\delta_{\alpha\beta}. \quad (17)$$

Here, we shall define a second-order polynomial based on the general discrete velocities  $v_{i\alpha} = \sqrt{\theta} c_{i\alpha} + u_\alpha$ ,

$$g_i^{\text{eq}} = W_i [M^{\text{eq}} + M_\alpha (v_{i\alpha} - u_\alpha) + M_{\alpha\beta} (v_{i\alpha} v_{i\beta} - \theta T_L \delta_{\alpha\beta} - u_\alpha u_\beta)], \quad (18)$$

where it can easily be observed that the zeroth-order moment is already recovered. To satisfy the higher order moments, we must solve for  $M_\alpha$  and  $M_{\alpha\beta}$ . Substituting (18) in (14) gives

$$q_\alpha^{\text{eq}} = M^{\text{eq}}u_\alpha + M_\alpha\theta T_L + 2\theta T_L M_{\alpha\beta}u_\beta, \quad (19)$$

$$R_{\alpha\beta}^{\text{eq}} = M^{\text{eq}}(\theta T_L\delta_{\alpha\beta} - u_\alpha u_\beta) + q_\alpha^{\text{eq}}u_\beta + q_\beta^{\text{eq}}u_\alpha + 2\theta^2 T_L^2 M_{\alpha\beta}. \quad (20)$$

Considering the explicit relations of the moments given by Eqs. (15)-(17) and taking into account the scaling  $\theta = p/\rho T_L$  one obtains

$$\begin{aligned} M_\alpha &= 0, \\ M_{\alpha\beta} &= \rho\delta_{\alpha\beta}. \end{aligned} \quad (21)$$

Finally, upon substitution in Eq. (18),  $g_i^{\text{eq}}$  is obtained as,

$$g_i^{\text{eq}} = \rho W_i \left[ 2e - D(p/\rho) + v_i^2 \right], \quad (22)$$

where  $D$  is the space dimension. As mentioned earlier, the source term  $G_i$  in Eq. (5) is responsible for correction of the energy equation. Here, we only attempt to derive the formulation as we will discuss the details later. To derive an expression for the correction term in the co-moving RF, we follow the same method employed to express  $g_i^{\text{eq}}$ . The pertinent moments of the correction term are,

$$M_0 = \sum_{i=0}^Q G_i^\lambda, \quad 0 = \sum_{i=0}^Q G_i^\lambda v_{i\alpha}, \quad 0 = \sum_{i=0}^Q G_i^\lambda v_{i\alpha} v_{i\beta}, \quad (23)$$

Using relations (19) and (20), one can write,

$$0 = M_0 u_\alpha + M_\alpha \theta T_L + 2\theta T_L M_{\alpha\beta} u_\beta, \quad (24)$$

$$0 = M_0 (\theta T_L \delta_{\alpha\beta} - u_\alpha u_\beta) + 2\theta^2 T_L^2 M_{\alpha\beta}, \quad (25)$$

which leads to the following solution,

$$\begin{aligned} M_\alpha &= -M_0 \frac{u^2}{\theta^2 T_L^2} u_\alpha, \\ M_{\alpha\beta} &= \frac{M_0}{2\theta^2 T_L^2} [u_\alpha u_\beta - \theta T_L \delta_{\alpha\beta}]. \end{aligned} \quad (26)$$

Eventually, we can write the polynomial form of the correction term as,

$$G_i^\lambda = M_0 W_i \left( 1 + \rho \frac{u_\alpha u_\beta c_{i\alpha} c_{i\beta}}{2p T_L} - \frac{\rho v_i^2}{2p} + \frac{D}{2} \right), \quad (27)$$

where  $M_0$  is the correction term in the energy equation.

### 2.1.1. Energy conservation in a non-ideal gas

In what follows, we briefly comment on the necessity of using the two-population approach as a result of modeling a generic, non-ideal gas. The recovery of the correct energy equation from the kinetic equations is crucial for modeling non-ideal fluids and in particular, two-phase systems with large variations of

density and temperature as encountered in supersonic flows with shocks. To that end, two-population approaches have long been used in the literature to split the conservation laws, where one population accounts for mass and momentum, whereas a separate population carries the total or internal energy only (see, e.g., [41] in the ideal-gas framework or [32] for multiphase flows). We remind that the internal energy of a non-ideal fluid is now a function of both density as well as the temperature,

$$de = C_v dT + \left[ T \left( \frac{\partial p}{\partial T} \right)_v - p \right] dv, \quad (28)$$

where  $C_v = (\partial e / \partial T)_v$  is the specific heat at constant volume and  $v = 1/\rho$  is the specific volume. One can evaluate that the second term on the RHS of Eq. (28) vanishes for an ideal-gas.

For the sake of presentation, we shall at first neglect the interface energy and only consider  $E = u^2/2 + e$ , where  $E$  is the total energy,  $e = e(s, v)$  is the local internal energy per unit of mass,  $s$  is the entropy and temperature is defined by  $T = (\partial e / \partial s)_v$ . The pressure tensor in our approach takes the form  $P_{\alpha\beta} = \rho u_\alpha u_\beta + p \delta_{\alpha\beta}$ , where  $p$  is the thermodynamic pressure corresponding to the chosen EOS. Accordingly, the trace of this tensor represents the total energy  $2\rho E = \rho u^2 + 2\rho e$  with

$$2\rho e = pD, \quad (29)$$

In the case of an ideal-gas, this reduces to  $e = DT$ , which, as expected, is only a function of temperature. Thus, equation (29) is fully valid for ideal gases with a fixed specific heat  $C_v = D/2$ . However, the internal energy of a real gas is a function of both density and temperature. In this paper, we use the classical van der Waals (vdW) EOS  $p = \rho RT / (1 - b\rho) - a\rho^2$  to model non-ideal behavior of real-gases but others can be used analogously. The constants are set to  $a = 2/49$ ,  $b = 2/21$  and  $R = 1$ , where  $a$  is the long-range attraction parameter,  $b$  represents the excluded-volume effect and  $R$  is the specific gas constant. Considering the vdW EOS, we have

$$\left( \frac{\partial e_{vdw}}{\partial \rho} \right)_T = T \left( \frac{\partial p}{\partial T} \right)_v - p = -a, \quad (30)$$

$$e_{vdw} = \int C_v dT - a\rho, \quad (31)$$

which suggests that  $e_{vdw} = F(T) - a\rho$ , where  $F(T)$  is an arbitrary function of temperature. In other words, the internal energy of a vdW fluid is the sum of a density-dependent function and temperature-dependent function. The same analogy can be applied to all EOS's with a linear dependence on the temperature and density-dependent tail part; such as Carnahan-Starling EOS. However, evaluating the internal energy of a vdW fluid using equation (29) (for  $D = 2$ ) yields,

$$\tilde{e}_{vdw} = \frac{p}{\rho} = \frac{RT}{1 - b\rho} - a\rho, \quad (32)$$

which is inconsistent with (31) since the first term depends on both, the density and the temperature. Hence, the pressure tensor alone cannot represent the total energy in general. This is only true for ideal gas. Consequently a second set of population is needed to represent the energy.

### 2.1.2. Correction of the energy equation

We must comment that the expression of heat flux recovered from the Chapman-Enskog analysis (see Section 2.2) without the correction term in the  $g$  population is found as  $q_\alpha^{\text{CE}} = -\mu \partial_\alpha h$  where  $\mu$  is the shear viscosity and  $h = e + p/\rho$  is the specific enthalpy. At the limit of an ideal-gas, this is equivalent to the

Fourier law  $q_\alpha^{\text{ig}} = -k_{\text{ig}}\partial_\alpha T$  where  $k_{\text{ig}} = \mu C_p^{\text{ig}}$  and hence the Prandtl number is fixed to  $\text{Pr} = \mu C_p^{\text{ig}}/k_{\text{ig}} = 1$  due to the single relaxation time BGK collision model. However, considering the enthalpy of a real-gas as a function of pressure and temperature, we have,  $\partial_\alpha h = C_p \partial_\alpha T + v(1 - \beta T)\partial_\alpha p$ , where  $\beta = v^{-1}(\partial v/\partial T)_p$  is the thermal expansion coefficient and  $C_p = C_v + Tv\beta(\partial p/\partial T)_v$  is the specific heat at constant pressure. While one could eliminate the pressure part of the enthalpy by the correction term and only retain the temperature dependent part, it must be noted that the thermal expansion coefficient *at* the critical point diverges,  $\beta \rightarrow \infty$  and so does the specific heat  $C_p \rightarrow \infty$ . Hence to recover the well-known Fourier law, the post-collision of the  $g$  population is augmented by the correction term  $G_i^\lambda \delta t$  where  $M_0 = \sum G_i^\lambda$  in Eq. (27) is set to  $M_0 = 2\partial_\alpha(-\mu\partial_\alpha h + k\partial_\alpha T)$  and  $k$  is the conductivity to be set independently.

### 2.1.3. Surface tension

In order to describe two-phase flows in the sub-critical part of the phase-diagram, the collision step for the  $f$ -populations (4) is augmented with a source (forcing) term  $S_i^\lambda$ ,

$$S_i^\lambda = G_{u+\delta u}^\mu[\rho W_i] - \rho W_i, \quad (33)$$

where  $\delta u = F/\rho\delta t$  is the change of the local flow velocity due to the force  $F_\alpha = \partial_\beta K_{\alpha\beta}$ , where

$$K_{\alpha\beta} = \kappa \left( \Delta\rho + \frac{1}{2}|\nabla\rho|^2 \right) \delta_{\alpha\beta} + \kappa\partial_\alpha\rho\partial_\beta\rho \quad (34)$$

is the Kortweg stress [8],  $\Delta = \nabla^2$  is the laplacian operator and  $\kappa$  is the surface tension coefficient. The first term on the R.H.S of equation (33) denotes the transformation of equilibrium populations residing at the reference frame " $u + \delta u$ " to the reference frame " $u$ " which could be realized as the Exact Difference Method (EDM) [42] adapted to the comoving RF. Having included the source term  $S_i$ , the actual fluid velocity is now shifted to  $\hat{u} = u + \delta u/2$  where  $u = 1/\rho \sum f_i v_i$ .

In the presence of the interface, the local equilibrium (22) is extended to account for the forcing  $F$ . In order to do that, the same analogy used in the absence of the force term is employed here with the only difference that the velocity terms in the pertinent moments (15)-(17) are replaced by the modified velocities,

$$\hat{u}_\alpha = u_\alpha + \frac{F_\alpha \delta t}{2\rho}, \quad (35)$$

With the new settings considered, the solution to relations (19) and (20) gives,

$$M_\alpha = \frac{1}{(p/\rho)} \left[ F_\alpha (\hat{H} - u^2) \delta t - \left[ u_\alpha \delta t + \left( \hat{H} + \frac{p}{\rho} \right) \frac{\delta t^2}{2p} F_\alpha \right] F_\beta u_\beta \right], \quad (36)$$

$$M_{\alpha\beta} = \rho \delta_{\alpha\beta} + \frac{\rho \delta t}{2p} [u_\alpha F_\beta + F_\alpha u_\beta] + \frac{\rho \delta t^2}{4p^2} F_\alpha F_\beta (\hat{H} + p/\rho), \quad (37)$$

which can be written in a compact form using the expression  $\hat{u}_\alpha F_\beta + \hat{u}_\beta F_\alpha = u_\alpha F_\beta + u_\beta F_\alpha + \delta t F_\alpha F_\beta / \rho$  and taking  $G_{\alpha\beta} = \hat{u}_\alpha F_\beta + \hat{u}_\beta F_\alpha + \delta t F_\alpha F_\beta \hat{E} / 2p$ ,

$$M_\alpha = \frac{\delta t}{(p/\rho)} [F_\alpha \hat{H} - G_{\alpha\beta} u_\beta], \quad (38)$$

$$M_{\alpha\beta} = \frac{1}{(p/\rho)} \left[ p \delta_{\alpha\beta} + \frac{\delta t}{2} G_{\alpha\beta} \right], \quad (39)$$

where  $\hat{H} = \hat{E} + p/\rho = h + \hat{u}^2/2$ . Finally, the extended equilibrium takes the form,

$$g_i^{eq} = W_i \left[ 2\rho\hat{E} + M_\alpha(v_{i\alpha} - u_\alpha) + M_{\alpha\beta} \left( v_{i\alpha}v_{i\beta} - \frac{p}{\rho}\delta_{\alpha\beta} - u_\alpha u_\beta \right) \right], \quad (40)$$

where  $\rho\hat{E} = \rho E + \hat{u}^2/2$  is based on the actual velocity of the flow. Note that in the absence of the force, the equilibrium (40) simplifies to Eq. (22). Consequently, the corresponding work of the added force is taken into account in the energy equation by modifying the correction term (27) with  $M_0 = 2\partial_\alpha(-\mu\partial_\alpha h + k\partial_\alpha T) + 2\hat{u}_\alpha\partial_\beta K_{\alpha\beta}$ . Finally, with the above modifications, the hydrodynamic equations for a two-phase system are recovered in its correct form. The evolution equations (69)-(71) together with the stress tensor (72) remain intact however, all the velocity terms  $\mathbf{u}$  are replaced by the actual velocity  $\hat{\mathbf{u}}$ . Furthermore, the standard form of the total-energy conservation for a two-phase system [43] is recovered,

$$\partial_t(\rho\hat{\mathcal{E}}) + \partial_\alpha(\rho\hat{\mathcal{E}}\hat{u}_\alpha + p\hat{u}_\alpha + \hat{\tau}_{\alpha\beta}\hat{u}_\beta + q_\alpha + K_{\alpha\beta}\hat{u}_\beta + \kappa\rho\partial_\beta\hat{u}_\beta\partial_\alpha\rho) = 0, \quad (41)$$

where  $\rho\hat{\mathcal{E}} = \rho\hat{E} + \frac{\kappa}{2}|\nabla\rho|^2$  accounts for the excess energy of the interface, as well.

It is essential to mention that the van der Waals formulation of a real-gas, features negative values of pressure for a range of temperatures in the subcritical region ( $T_r < 0.84375$ ) where a constant base-pressure must be added in order to have a meaningful evaluation of discrete velocities (1). To resolve this issue, we redefine the pressure as  $p = p_{vdw} + \bar{p}$  which is positive. This will contribute to the internal energy according to relation (28), where the pressure-dependent part is reevaluated as,

$$T \left( \frac{\partial p}{\partial T} \right)_v - p = \frac{a}{v^2} - \bar{p}. \quad (42)$$

Finally, the internal energy of a vdW fluid with base-pressure  $\bar{p}$  and constant specific heat  $C_v$  is derived,

$$e = C_v T - a\rho - \frac{\bar{p}}{\rho}. \quad (43)$$

However, the enthalpy of such a fluid remains intact since,

$$h = e + \frac{p_{vdw} + \bar{p}}{\rho}, \quad (44)$$

$$h = C_v T - a\rho + \frac{p_{vdw}}{\rho} - \frac{\bar{p}}{\rho} + \frac{\bar{p}}{\rho}, \quad (45)$$

where the effect of the base-pressure is cancelled out in evaluation of the enthalpy.

## 2.2. Chapman-Enskog analysis

### 2.2.1. Excluding the forcing term

Here we aim at recovering the macroscopic Navier-Stokes equations from the dynamics of kinetic equations (2-5). To this end, the pertinent equilibrium moments of  $f$  and  $g$  populations are required, which are computed as follows:

$$P_{\alpha\beta}^{eq} = \sum_{i=0}^Q f_i^{eq} v_{i\alpha} v_{i\beta} = \rho u_\alpha u_\beta + p \delta_{\alpha\beta}, \quad (46)$$

$$Q_{\alpha\beta\gamma}^{eq} = \sum_{i=0}^Q g_i^{eq} v_{i\alpha} v_{i\beta} v_{i\gamma} = \rho u_\alpha u_\beta u_\gamma + p [u\delta]_{\alpha\beta\gamma}, \quad (47)$$

$$q_\alpha^{eq} = \sum_{i=0}^Q g_i^{eq} v_{i\alpha} = 2\rho u_\alpha H, \quad (48)$$

$$R_{\alpha\beta}^{eq} = \sum_{i=0}^Q g_i^{eq} v_{i\alpha} v_{i\beta} = 2\rho u_\alpha u_\beta (H + p/\rho) + 2pH\delta_{\alpha\beta}, \quad (49)$$

where  $[u\delta]_{\alpha\beta\gamma} = u_\alpha \delta_{\beta\gamma} + u_\beta \delta_{\alpha\gamma} + u_\gamma \delta_{\alpha\beta}$  and  $H$  is the total enthalpy. First, we introduce the following expansions:

$$f_i = f_i^{(0)} + \epsilon f_i^{(1)} + \epsilon^2 f_i^{(2)}, \quad (50)$$

$$g_i = g_i^{(0)} + \epsilon g_i^{(1)} + \epsilon^2 g_i^{(2)}, \quad (51)$$

$$\partial_t = \epsilon \partial_t^{(1)} + \epsilon^2 \partial_t^{(2)}, \quad (52)$$

$$\partial_\alpha = \epsilon \partial_\alpha^{(1)}. \quad (53)$$

Applying the Taylor expansion up to second order and separating the orders of  $\epsilon$  results in:

$$\{f_i^{(0)}, g_i^{(0)}\} = \{f_i^{eq}, g_i^{eq}\}, \quad (54)$$

$$\partial_t^{(1)} \{f_i^{(0)}, g_i^{(0)}\} + v_{i\alpha} \partial_\alpha^{(1)} \{f_i^{(0)}, g_i^{(0)}\} = -(\omega/\delta t) \{f_i^{(1)}, g_i^{(1)}\}, \quad (55)$$

$$\begin{aligned} \partial_t^{(2)} \{f_i^{(0)}, g_i^{(0)}\} + \left( \partial_t^{(1)} + v_{i\alpha} \partial_\alpha^{(1)} \right) (1 - \frac{\omega}{2}) \{f_i^{(1)}, g_i^{(1)}\} \\ = -(\omega/\delta t) \{f_i^{(2)}, g_i^{(2)}\}. \end{aligned} \quad (56)$$

The local conservation of density, momentum and energy imply

$$\sum_{i=0}^Q \{f_i^{(n)}, g_i^{(n)}\} = 0, n \geq 1, \quad (57)$$

$$\sum_{i=0}^Q f_i^{(n)} v_{i\alpha} = 0, n \geq 1 \quad (58)$$

Applying conditions (57) and (58) on equation (55), we derive the following first order equations,

$$D_t^{(1)}\rho = -\rho\partial_\alpha^{(1)}u_\alpha, \quad (59)$$

$$D_t^{(1)}u_\alpha = -\frac{1}{\rho}\partial_\alpha^{(1)}p, \quad (60)$$

$$D_t^{(1)}T = -\frac{T}{\rho C_v} \left( \frac{\partial p}{\partial T} \right)_\rho \partial_\alpha^{(1)}u_\alpha, \quad (61)$$

where  $D_t^{(1)} = \partial_t^{(1)} + u_\alpha\partial_\alpha^{(1)}$  is the first order total-derivative. Subsequently, we can derive a similar equation for pressure considering that  $p = p(\rho, T)$ . This yields

$$D_t^{(1)}p = \left( \frac{\partial p}{\partial \rho} \right)_T D_t^{(1)}\rho + \left( \frac{\partial p}{\partial T} \right)_\rho D_t^{(1)}T = -\rho\varsigma^2\partial_\alpha^{(1)}u_\alpha, \quad (62)$$

where  $\varsigma = \sqrt{\left( \frac{\partial p}{\partial \rho} \right)_s}$  is the speed of sound given by,

$$\varsigma = \sqrt{\left( \frac{\partial p}{\partial \rho} \right)_T + \frac{T}{\rho^2 c_v} \left( \frac{\partial p}{\partial T} \right)_\rho^2}. \quad (63)$$

The second order relations are obtained by applying the conditions (57) and (58) to equation (56),

$$\partial_t^{(2)}\rho = 0, \quad (64)$$

$$\partial_t^{(2)}u_\alpha = \frac{1}{\rho}\partial_\beta^{(1)} \left[ \delta t \left( \frac{1}{\omega} - \frac{1}{2} \right) \left( \partial_t^{(1)}P_{\alpha\beta}^{eq} + \partial_\gamma^{(1)}Q_{\alpha\beta\gamma}^{eq} \right) \right], \quad (65)$$

$$\partial_t^{(2)}T = \frac{1}{2\rho C_v} \left\{ \partial_\alpha^{(1)} \left[ \delta t \left( \frac{1}{\omega} - \frac{1}{2} \right) \left( \partial_t^{(1)}q_\alpha^{eq} + \partial_\beta^{(1)}R_{\alpha\beta}^{eq} \right) \right] - 2\rho u_\alpha \partial_t^{(2)}u_\alpha \right\}. \quad (66)$$

Equations (59) and (64) constitute the continuity equation. The non-equilibrium pressure tensor and heat flux in the R.H.S of equations (65) and (66) are evaluated using equations (59-62),

$$\partial_t^{(1)}P_{\alpha\beta}^{eq} + \partial_\gamma^{(1)}Q_{\alpha\beta\gamma}^{eq} = p \left( \partial_\beta^{(1)}u_\alpha + \partial_\alpha^{(1)}u_\beta \right) + \left( p - \rho\varsigma^2 \right) \partial_\gamma^{(1)}u_\gamma \delta_{\alpha\beta} \quad (67)$$

$$\partial_t^{(1)}q_\alpha^{eq} + \partial_\beta^{(1)}R_{\alpha\beta}^{eq} = 2 \left( p - \rho\varsigma^2 \right) \partial_\gamma^{(1)}u_\gamma u_\alpha + 2p u_\beta \left( \partial_\beta^{(1)}u_\alpha + \partial_\alpha^{(1)}u_\beta \right) + 2p\partial_\alpha^{(1)}h \quad (68)$$

Finally, summing up the contributions of density, momentum and temperature at the  $\epsilon$  and  $\epsilon^2$  orders and taking into account the correction to the energy equation (27), we get the hydrodynamic limit of the model, which reads

$$D_t\rho = -\rho\partial_\alpha u_\alpha, \quad (69)$$

$$\rho D_t u_\alpha = -\partial_\alpha p - \partial_\beta \tau_{\alpha\beta}, \quad (70)$$

$$\rho C_v D_t T = -\tau_{\alpha\beta} \partial_\alpha u_\beta - T \left( \frac{\partial p}{\partial T} \right)_v \partial_\alpha u_\alpha - \partial_\alpha q_\alpha, \quad (71)$$

where  $D_t = \partial_t + u_\alpha \partial_\alpha$  is the material derivative,  $q_\alpha = -k\partial_\alpha T$  is the heat flux and the nonequilibrium stress tensor reads,

$$\tau_{\alpha\beta} = -\mu \left( \partial_\alpha u_\beta + \partial_\beta u_\alpha - \frac{2}{D} (\partial_\gamma u_\gamma) \delta_{\alpha\beta} \right) - \eta (\partial_\gamma u_\gamma) \delta_{\alpha\beta}. \quad (72)$$

The shear and bulk viscosity are,

$$\mu = \left( \frac{1}{\omega} - \frac{1}{2} \right) p \delta t, \quad (73)$$

$$\eta = \left( \frac{1}{\omega} - \frac{1}{2} \right) \left( \frac{D+2}{D} - \frac{\rho \zeta^2}{p} \right) p \delta t, \quad (74)$$

respectively and  $\zeta = \sqrt{(\partial p / \partial \rho)_s}$  is the speed of sound. As expected, the bulk viscosity vanishes in the limit of ideal monatomic gas. Furthermore, one can observe that only the excluded volume part of the pressure  $T(\partial p / \partial T)_v$  contributes to the temperature equation (71), as expected.

### 2.2.2. Including the forcing term

As mentioned before, the force terms in the kinetic equations represent the interface dynamics. First, we recast the post-collision state of the  $f$  population in the following form [44],

$$f_i^*(\mathbf{x}, t) = f_i(\mathbf{x}, t) + \omega (f_i^{eq}(\rho, \hat{\mathbf{u}}) - f_i(\mathbf{x}, t)) + \hat{S}_i, \quad (75)$$

$$\hat{\mathbf{u}} = \mathbf{u} + \frac{\mathbf{F} \delta t}{2\rho}, \quad (76)$$

$$\hat{S}_i = S_i - \omega \left( f_i^{eq}(\rho, \hat{\mathbf{u}}) - \rho W_i \right), \quad (77)$$

where  $[S_i = f_i^{eq}(\rho, \mathbf{u} + \mathbf{F} \delta t / \rho) - \rho W_i]$  and  $F_\alpha = -\partial_\beta K_{\alpha\beta}$ . Here we expand the forcing term  $\hat{S}_i^{(1)} = \epsilon \hat{S}_i^{(1)}$  in addition to the expansions (50,52,53). Similarly, we get the following relations at the orders of  $\epsilon^0, \epsilon^1, \epsilon^2$  respectively,

$$f_i^{(0)} = f_i^{eq}(\rho, \hat{\mathbf{u}}), \quad (78)$$

$$\partial_t^{(1)} f_i^{(0)} + v_{i\alpha} \partial_\alpha^{(1)} f_i^{(0)} = -(\omega / \delta t) f_i^{(1)} + \frac{1}{\delta t} \hat{S}_i^{(1)}, \quad (79)$$

$$\partial_t^{(2)} f_i^{(0)} + \left( \partial_t^{(1)} + v_{i\alpha} \partial_\alpha^{(1)} \right) \left( 1 - \frac{\omega}{2} \right) f_i^{(1)} + \frac{1}{2} \left( \partial_t^{(1)} + v_{i\alpha} \partial_\alpha^{(1)} \right) \hat{S}_i^{(1)} = -(\omega / \delta t) f_i^{(2)}, \quad (80)$$

It is important here to assess the solvability conditions imposed by the local conservations. Considering the moment-invariant property of the transfer matrix between the two gauges  $\lambda = \{p/\rho, \mathbf{u}\}$  and  $\hat{\lambda} = \{p/\rho, \hat{\mathbf{u}}\}$ , one can easily compute,

$$\sum_{i=0}^Q f_i^{(0)} = \sum_{i=0}^Q f_i^{eq}(\rho, \hat{\mathbf{u}}) = \rho, \quad (81)$$

$$\sum_{i=0}^Q f_i^{(0)} v_{i\alpha} = \sum_{i=0}^Q f_i^{eq}(\rho, \hat{\mathbf{u}}) v_{i\alpha} = \rho \hat{u}_\alpha. \quad (82)$$

This implies that,

$$\sum_{i=0}^Q f_i^{(n)} = 0, n \geq 1, \quad (83)$$

$$\sum_{i=0}^Q f_i^{(n)} v_{i\alpha} = \begin{cases} -\frac{\delta t}{2} F_\alpha^{(1)}, & n=1 \\ 0, & n>1 \end{cases} \quad (84)$$

According to the definition of  $S_i$ , the following moments can be computed:

$$\sum_{i=0}^Q \hat{S}_i^{(1)} = 0, \quad (85)$$

$$\sum_{i=0}^Q \hat{S}_i^{(1)} v_{i\alpha} = \delta t \left(1 - \frac{\omega}{2}\right) F_\alpha^{(1)}, \quad (86)$$

$$\sum_{i=0}^Q \hat{S}_i^{(1)} v_{i\alpha} v_{i\beta} = \delta t \left(1 - \frac{\omega}{2}\right) (\hat{u}_\alpha F_\beta + \hat{u}_\beta F_\alpha) + \frac{\omega \delta t^2 F_\alpha F_\beta}{4\rho}. \quad (87)$$

Similarly, the first order equations of density and momentum are derived by applying the solvability conditions (83) and (84) on equations (79) and (80),

$$\hat{D}_t^{(1)} \rho = -\rho \partial_\alpha^{(1)} \hat{u}_\alpha, \quad (88)$$

$$\hat{D}_t^{(1)} \hat{u}_\alpha = -\frac{1}{\rho} \partial_\alpha^{(1)} p + \frac{1}{\rho} F_\alpha^{(1)}, \quad (89)$$

where  $\hat{D}_t^{(1)} = \partial_t^{(1)} + \hat{u}_\alpha \partial_\alpha^{(1)}$ . At this point it is necessary to mention that since there is a force added to the momentum equation (in this case the divergence of the Korteweg stress), it should also be considered in the energy equation as well. Hence as mentioned before,  $M_0$  in Eq. (27) is modified to,

$$M_0 = 2\partial_\alpha (-\mu \partial_\alpha h + k \partial_\alpha T) + 2\hat{u}_\alpha F_\alpha. \quad (90)$$

The equilibrium moments are modified as,

$$\sum_{i=0}^Q g_i^{eq} = 2\rho \hat{E}, \quad (91)$$

$$q_\alpha^{eq} = \sum_{i=0}^Q g_i^{eq} v_{i\alpha} = 2\rho \hat{u}_\alpha \hat{H}, \quad (92)$$

$$R_{\alpha\beta}^{eq} = \sum_{i=0}^Q g_i^{eq} v_{i\alpha} v_{i\beta} = 2\rho \hat{u}_\alpha \hat{u}_\beta (\hat{H} + p/\rho) + 2p \hat{H} \delta_{\alpha\beta}, \quad (93)$$

where  $\hat{E} = e + \hat{u}^2/2$  and  $\hat{H} = \hat{E} + p/\rho$ . With the changes mentioned so far, the first-order equation of temperature is derived as

$$\hat{D}_t^{(1)} T = -\frac{T}{\rho C_v} \left( \frac{\partial p}{\partial T} \right)_\rho \partial_\alpha^{(1)} \hat{u}_\alpha. \quad (94)$$

Finally, in a similar manner as the case without the force, the macroscopic equations are recovered by collecting the equations of density, momentum and temperature at each order,

$$\hat{D}_t \rho = -\rho \partial_\alpha \hat{u}_\alpha, \quad (95)$$

$$\rho \hat{D}_t \hat{u}_\alpha = -\partial_\alpha p - \partial_\beta \hat{\tau}_{\alpha\beta} - \partial_\beta K_{\alpha\beta}, \quad (96)$$

$$\rho C_v \hat{D}_t T = -\hat{\tau}_{\alpha\beta} \partial_\alpha \hat{u}_\beta - T \left( \frac{\partial p}{\partial T} \right)_v \partial_\alpha \hat{u}_\alpha - \partial_\alpha q_\alpha, \quad (97)$$

$$\hat{\tau}_{\alpha\beta} = -\mu \left( \partial_\alpha \hat{u}_\beta + \partial_\beta \hat{u}_\alpha - \frac{2}{D} (\partial_\gamma \hat{u}_\gamma) \delta_{\alpha\beta} \right) - \eta (\partial_\gamma \hat{u}_\gamma) \delta_{\alpha\beta}. \quad (98)$$

It should be noted that the error terms associated with the forcing are not shown here. For instance, as reported in the literature [44–46] one can show that the error term in the momentum equation appears as  $\nabla \cdot (\delta t^2 \mathbf{F}\mathbf{F}/4\rho)$ .

The total energy of the fluid is formulated by  $\hat{\mathcal{E}} = e(T, v) + \hat{u}^2/2 + E_\lambda$  where  $E_\lambda = \kappa |\nabla \rho|^2/2$  is the non-local part corresponding to the excess energy of the interface. The evolution equation for the specific internal energy  $e(T, v)$  can be obtained by considering equations (28,95,97)

$$\rho \hat{D}_t e = -p \partial_\alpha \hat{u}_\alpha - \hat{\tau}_{\alpha\beta} \partial_\alpha \hat{u}_\beta - \partial_\alpha q_\alpha. \quad (99)$$

From the momentum equation (96) we get,

$$\frac{1}{2} \rho \hat{D}_t \hat{u}^2 = -\hat{u}_\alpha \partial_\alpha p - \hat{u}_\alpha \partial_\beta \hat{\tau}_{\alpha\beta} - \hat{u}_\alpha \partial_\beta K_{\alpha\beta}, \quad (100)$$

and the evolution of the excess energy can be computed using the continuity equation,

$$\rho \hat{D}_t E_\lambda = -K_{\alpha\beta} \partial_\beta \hat{u}_\alpha - \partial_\alpha (\kappa \rho \partial_\beta \hat{u}_\beta \partial_\alpha \rho). \quad (101)$$

by summing up the contribution of each three part we get the full conservation equation for the total energy,

$$\partial_t (\rho \hat{\mathcal{E}}) + \partial_\alpha \left( \rho \hat{\mathcal{E}} \hat{u}_\alpha + p \hat{u}_\alpha + \hat{\tau}_{\alpha\beta} \hat{u}_\beta + K_{\alpha\beta} \hat{u}_\beta + \kappa \rho \partial_\beta \hat{u}_\beta \partial_\alpha \rho + q_\alpha \right) = 0. \quad (102)$$

### 3. Results and discussion

In this section, we show validity of our model in a broad range of challenging problems, which are chosen to probe the correct thermodynamics as well as Galilean invariance:

- As a first test of basic thermodynamic consistency for non-ideal fluids, we simulate the inversion line of a vdW fluid, which is one of the classic thermodynamical concepts of non-ideal fluids. To capture this phenomenon it is crucial that the model recovers the correct energy equation and can operate in a wide range of pressures and temperatures in the super-critical part of the phase diagram.
- Phase-change is the next fundamental process that is tested with our model. It is important to remind that since the full energy equation is recovered by our kinetic equations, phase-change emerges naturally in the proposed scheme and no additional *ad-hoc* phase-change model is required. In addition, we probe fast dynamics with temperatures near the critical point, where phase-change happens in short time-scales.
- As a final test case we probe both thermodynamic consistency as well as Galilean invariance in supersonic flows. In particular, we study the behavior of a perturbed shock-front in both an ideal-gas

as well as a vdW fluids at Mach number  $Ma=3$ . In agreement with theory our model shows to capture all regimes, including the exotic behaviors of a real fluid.

### 3.1. Inversion line

When a fluid passes through a throttling device, the value of the enthalpy remains constant in the absence of work and heat. During this so-called throttling process, the pressure of the fluid drops and the behavior of the temperature is characterized by the well-known Joule-Thomson coefficient  $\mu = (\partial T / \partial P)_h$ . Depending on the sign and value of this coefficient, the temperature may increase, decrease or remain the constant through the process. It is trivial to talk about the ideal-gas assumption here since the coefficient is zero by definition and the temperature of an ideal-gas will thus not change. On the other hand, for real gases, we need to distinguish between three different regions in the  $T - P$  diagram, corresponding to the different signs of the Joule-Thomson coefficient. Hence, let us start by defining the inversion line as the locus of points where  $\mu = 0$ . Hence, crossing the inversion line will lead to a change of sign of  $\mu$ . For the vdW EOS, one can derive the expression for the inversion line as

$$P_r = 24\sqrt{3T_r} - 12T_r - 27, \quad (103)$$

where the subscript "r" indicates that the quantities are reduced with respect to their values at the critical point. The critical values of pressure, temperature and density for a vdW fluid are  $P_{cr} = a/27b^2$ ,  $T_{cr} = 8a/27Rb$  and  $\rho_{cr} = 1/3b$ , respectively. In addition to the reduced variables, it is useful to define the non-dimensional enthalpy as,

$$\hat{h} = \frac{h}{RT_{cr}} = T_r \left[ \frac{1}{\delta} + \frac{3}{3 - \rho_r} \right] - \frac{9}{4}\rho_r, \quad (104)$$

where  $\delta = R/C_v$  is a constant. A closer assessment of (103) reveals that the point with the maximum pressure on the inversion line has the following quantities  $(P_r, \rho_r, T_r, \hat{h}) = (9.0, 1.0, 3.0, 11.25)$ .

To test that our model captures these phenomena also numerically, we measure the value of Joule-Thomson coefficient at different points in the  $T - P$  diagram. This will then allow us to infer the inversion line, which can be compared to its analytical solution. We do this in two steps: in a first simulation the flow is subjected to a positive acceleration under fixed density; hence the pressure drops and the quantity  $(\partial P / \partial T)_\rho$  is measured. In a second simulation, the isothermal speed of sound  $(\partial P / \partial \rho)_T$  is computed by introducing a very small perturbation in the pressure field and measuring the velocity of the subsequent shock front. The Joule-Thomson coefficient may now be computed by,

$$\mu = -\frac{1}{C_p} \left[ \frac{1}{\rho} - T \frac{(\partial P / \partial T)_\rho}{\rho^2 (\partial P / \partial \rho)_T} \right], \quad (105)$$

where  $C_p$  is the specific heat at constant pressure. Finally, we use a simple Euler scheme to construct the isenthalpic lines with,

$$\Delta T \approx \mu \Delta P. \quad (106)$$

The simulations are conducted for three different enthalpies,  $\hat{h} = 5$ ,  $\hat{h} = 11.25$  and  $\hat{h} = 15$ . Figure 2 shows the measured values of the dimensionless Joule-Thomson coefficient at different reduced pressures up to the far supercritical value  $P_r = 15$ . The comparison between the van der Waals theory and the simulation is excellent and thus validates our scheme.

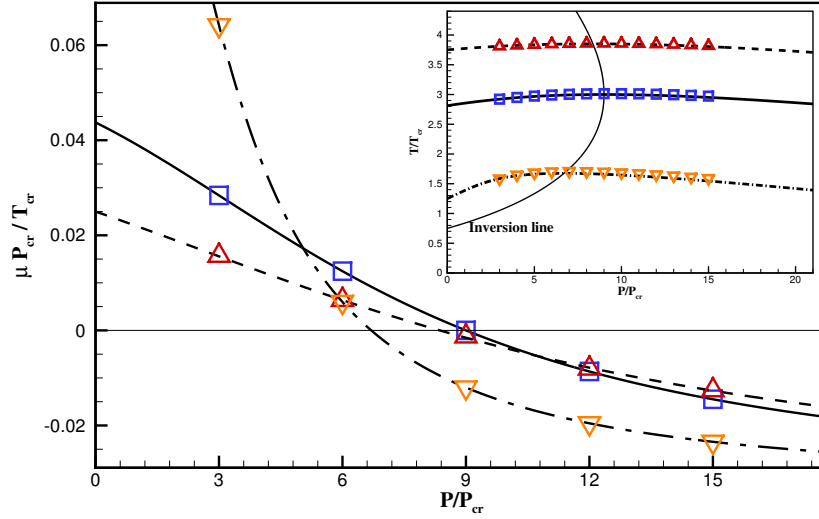


**Figure 2.** Joule-Thomson coefficient against reduced pressure. The value of the Joule-Thomson coefficient along the dimensionless isenthalpic lines  $\hat{h} = h/RT_{cr}$  was measured at a wide range of reduced pressures up to  $P/P_{cr} = 15$ . Line: theory; Solid:  $\hat{h} = 11.25$ ; Dashed:  $\hat{h} = 15$ ; Dash dot:  $\hat{h} = 5$ . Symbols: present method; Squares:  $\hat{h} = 11.25$ ; Triangles:  $\hat{h} = 15$ ; Inverted triangles:  $\hat{h} = 5$ . Inset: simulated lines of constant enthalpy on the  $T_r - P_r$  (phase) diagram.

### 3.2. Phase change: one dimensional Stefan problem

In this section, we validate our model for phase-change problems, starting from the one dimensional Stefan problem, where a liquid-vapor system is subjected to a heated wall on the vapor side. The heat transfer from the wall leads to evaporation of liquid and the interface is moving away from the wall. The analytical solution for the liquid-vapor interface location with time is given by  $x_i(t) = 2\beta\sqrt{\alpha_v t}$ , where  $\alpha_v$  is the diffusivity of the vapor and  $\beta$  is the solution to [47]

$$\beta \exp(\beta^2) \operatorname{erf}(\beta) = \frac{St}{\sqrt{\pi}}, \quad (107)$$

where  $St = C_{pv}\Delta T/h_{fg}$  is the Stefan number,  $C_{pv}$  is the specific heat capacity of the vapor phase,  $\Delta T$  is the temperature difference between the wall and the saturation temperature and  $h_{fg}$  denotes the latent heat of evaporation. Simulations have been carried out for three different Stefan numbers at fixed diffusivity. The choice of the Stefan number is directly related to the velocity of the interface:

$$u_i(t) = \frac{d}{dt}x_i(t) = \beta\sqrt{\frac{\alpha_v}{t}} \quad (108)$$

and hence the Mach number of the flow. Note that since our model is not restricted to low-speed flows, we can accurately capture a wide range of Stefan numbers. Figure (3) shows the location of the interface during evaporation compared to the analytical solution. The results of the simulation are in good agreement with the theory. We shall mention that the choice of parameters in our model such as the latent heat of evaporation  $h_{fg}$  or the specific heat  $C_p$  is not arbitrary and they are computed based on the thermodynamical state of the initial flow. For instance, the value of the Stefan number increases for a

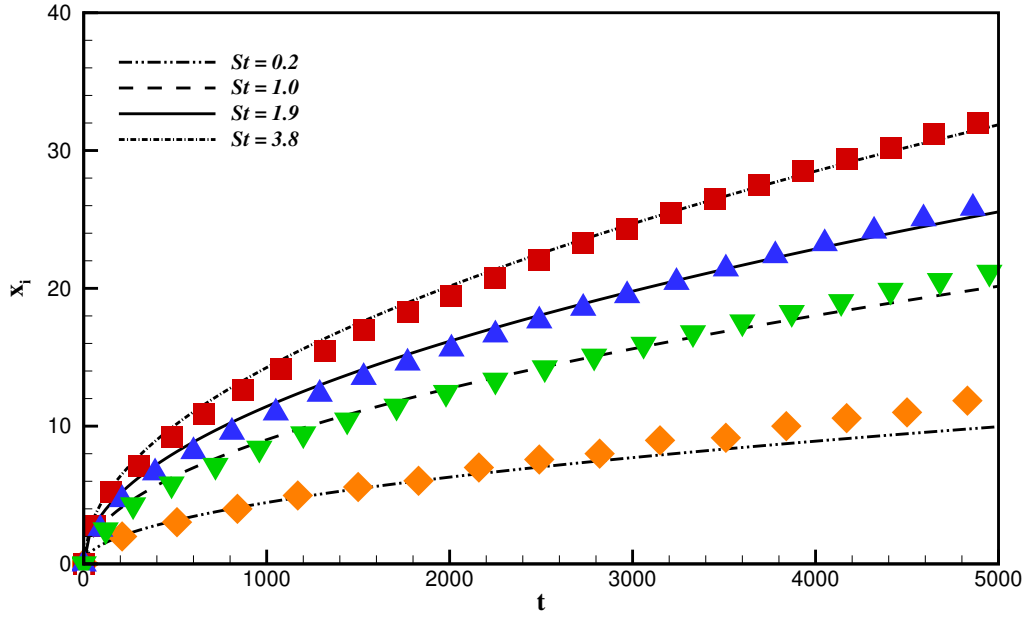


**Figure 3.** Location of the interface versus time in lattice units for three different Stefan numbers. Line: analytical solution. Symbols: present method.

given temperature difference  $\Delta T$  as we approach the critical point due to vanishing of  $h_{fg}$  and diverging of  $C_p$  at the critical point.

### 3.3. Phase change: nucleate boiling

Due to its importance in engineering and real life applications, boiling and its various regimes have always been the focus of many studies, both numerically and theoretically [43,48,49].

To validate our model, we choose a two dimensional setup where a liquid is in direct contact with a wall with high temperature at the middle of the wall. The schematic of the setup is shown in Fig. 4a. The non-uniform temperature of the wall triggers a two dimensional flow and the nucleus starts to appear and rise under the gravitational field. The nucleus continues to rise and grow until the necking is achieved where the bubble is detaching from the nucleus. Once the first bubble is detached from the nucleus and released into the liquid, the nucleus continues to grow and releases a second bubble. This is a periodic process of bubble release, which is a function of surface tension, density ratio and the gravity. An empirical correlation for the bubble release frequency was found experimentally by Zuber [50] and reads:

$$f^{-1} \approx \frac{d}{0.59} \left( \frac{\sigma g (\rho_l - \rho_v)}{\rho_l^2} \right)^{-1/4} \quad (109)$$

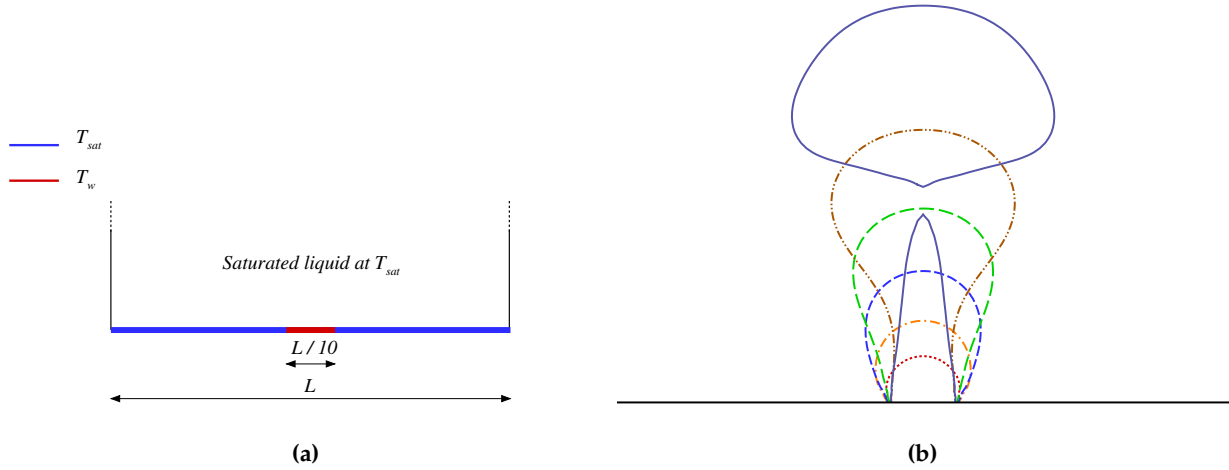


**Figure 4.** (a) Schematic of the nucleate problem. (b) The interface of the vapor bubble during the nucleation, starting from the appearance of the first nucleus until the release of the first bubble. From bottom to top; Fine-dashed: time=600, Dash dot: time = 1200, Dashed: time=1800, Long-dashed: time=2400, Dash dot-dot: time=3000, Solid: time=3780. Times are measured in lattice units.

where  $d$  is the departure diameter and itself proportional to  $g^{-0.5}$  [51]. Hence, the bubble release period is proportional to  $g^{-0.75}$ . We consider domain of  $121 \times 601$  points with time step  $\delta t = 0.3$ , conductivity  $k = 0.6$ , specific heat  $C_v = 3$ , viscosity  $\nu = 0.005$ , surface tension coefficient  $\kappa = 0.0234$  and gravity  $g = 0.0001$  in lattice units. The Jacob number is defined as

$$Ja = \frac{C_{pl}(T_w - T_{sat})}{h_{fg}}, \quad (110)$$

where  $C_{pl}$  is the specific heat of the liquid phase. The wall temperature is set to  $T_w = 1.5T_{sat}$ , where  $T_{sat}$  is the saturation temperature and the initial temperature of the liquid is  $T_{sat} = 0.9T_{cr}$ , which fixes the latent heat of evaporation. This choice of parameters leads to the Jacob number  $Ja = 2.21$ . Figure 4 b illustrates a sequence of the bubble interface from the early times of the first nucleus development until the first bubble is released into the liquid. The bubble release period was measure for different values of gravity and the results are presented in in Fig. (5). The comparison shows that our numerical simulations agree well with the empirical correlation.

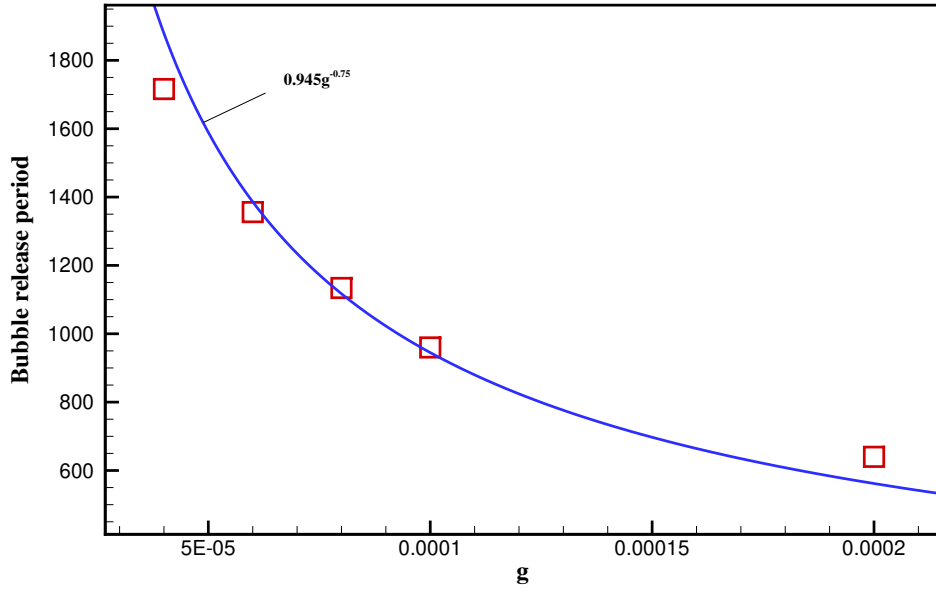


Figure 5. Bubble release period against different gravity numbers. Symbols: Simulation.

#### 3.4. Phase change: Single-mode film boiling

As a final phase-change validation, we conduct simulations of film boiling, where a heated horizontal surface is covered by a thin layer of vapor. The liquid rests on top of the vapor and both phases are initially saturated. Phase-change then takes place at the liquid-vapor interface, where the heat is transported from the hot wall with temperature  $T_w$ , which is set to be above its saturation temperature  $T_{sat}$ . The governing non-dimensional numbers are the Jacob, Prandtl and the Grashof number [52],

$$Ja = \frac{C_{pv}(T_w - T_{sat})}{h_{fg}}, \quad (111)$$

$$Pr = \frac{\mu_v C_{pv}}{k_v}, \quad (112)$$

$$Gr = \rho_v g (\rho_l - \rho_v) \frac{l_s^3}{\mu_v^2}, \quad (113)$$

defined for the vapor phase.  $l_s$  is the non-dimensional capillary length defined as,

$$l_s = \sqrt{\frac{\sigma}{(\rho_l - \rho_v)g}}, \quad (114)$$

and  $t^* = t/\sqrt{l_s/g}$  is the dimensionless time. The well-known experimental correlation as proposed in Klimenko [53] has the following form in the laminar flow regime ( $Gr \leq 4.03 \times 10^5$ ),

$$Nu = 0.1691 \left( \frac{GrPr}{Ja} \right)^{1/3}, \quad Ja < 0.71, \quad (115)$$

$$Nu = 0.19 (GrPr)^{1/3}, \quad Ja \geq 0.71, \quad (116)$$

where  $Nu$  is the Nusselt number. In our simulation, we consider domain of  $129 \times 257$  points with  $\delta t = 0.3$ ,  $k = 0.6$ ,  $C_v = 3$ ,  $\nu = 0.005$ ,  $\kappa = 0.0234$  and  $g = 0.0001$  in lattice units. The non-dimensional numbers are  $Ja = 0.064$ ,  $Pr = 0.094$  and  $Gr = 2482.58$ . Based on the value of the Jacob number, the Nusselt number as

computed from the correlation (115) amounts to  $Nu_k = 2.6085861$ . Initially, the liquid-vapor interface is perturbed with the function

$$y = 0.125W - 0.05W \cos\left(\frac{2\pi x}{W}\right), \quad (117)$$

where  $W$  is the width of the domain. The space-averaged Nusselt number is computed throughout the simulation using

$$\langle Nu \rangle = -\frac{l_s}{W(T_w - T_{sat})} \int_0^W \frac{\partial T}{\partial y} \Big|_w dx, \quad (118)$$

where the gradient of the temperature is computed at the wall using finite differences. The evolution of the liquid-vapor interface is shown at three different times in Fig. 6. The first bubble is released at  $t^* \approx 15$ , which is then followed by a periodic release of bubbles. The space-averaged Nusselt number is computed during the simulations until the first bubble is released. The results are presented in Fig. 7, where we have compared the time-averaged Nusselt number with the correlation (115). We can confirm the time-averaged Nusselt number is in very close agreement with the experimental correlation while according to [53], there is an acceptable  $\pm 25\%$  margin on the correlation.

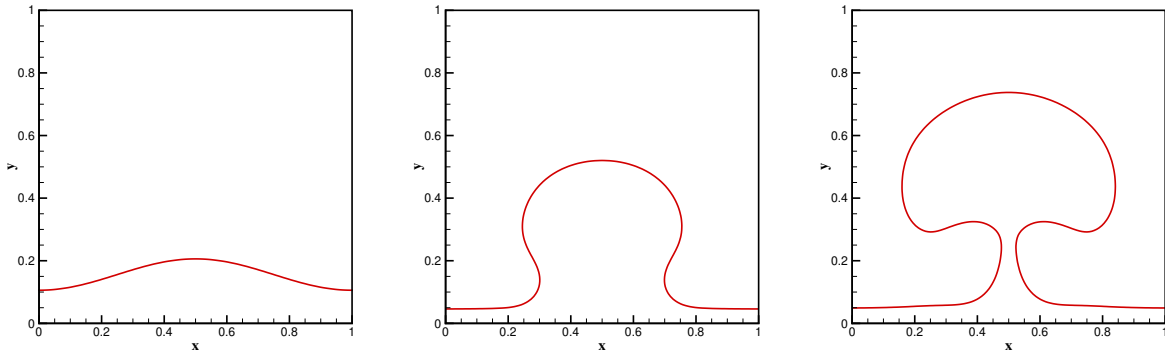


**Figure 6.** Bubble growth from the vapor film at  $Gr = 2482.58$ ,  $Ja = 0.064$  and  $Pr = 0.094$ . The phase boundary is shown at different times. From left to right:  $t^* = 0$ ,  $t^* = 9.8$ ,  $t^* = 14.96$

### 3.5. On the stability of the shock waves

The stability of planar shock waves subject to small perturbations have long been investigated since the pioneering work of D'yakov [54] and later modifications of Kontorovich [55], which were the first attempts to study the conditions under which a planar shock with corrugations on its surface would become unstable. The key parameter in the analysis of shock instabilities is the so called "D'yakov parameter" [18], defined as

$$h_D = j^2 \left( \frac{dv}{dp} \right)_H, \quad (119)$$

evaluated at the post-shock (downstream) state, where  $j^2 = (p_1 - p_0)/(v_0 - v_1)$  is the square of the mass flux across the shock front,  $v$  is the specific volume,  $p$  is the thermodynamic pressure and the subscript  $H$  denotes that the derivative is taken along the "Hugoniot" curve. Furthermore, the subscripts "0" and "1"

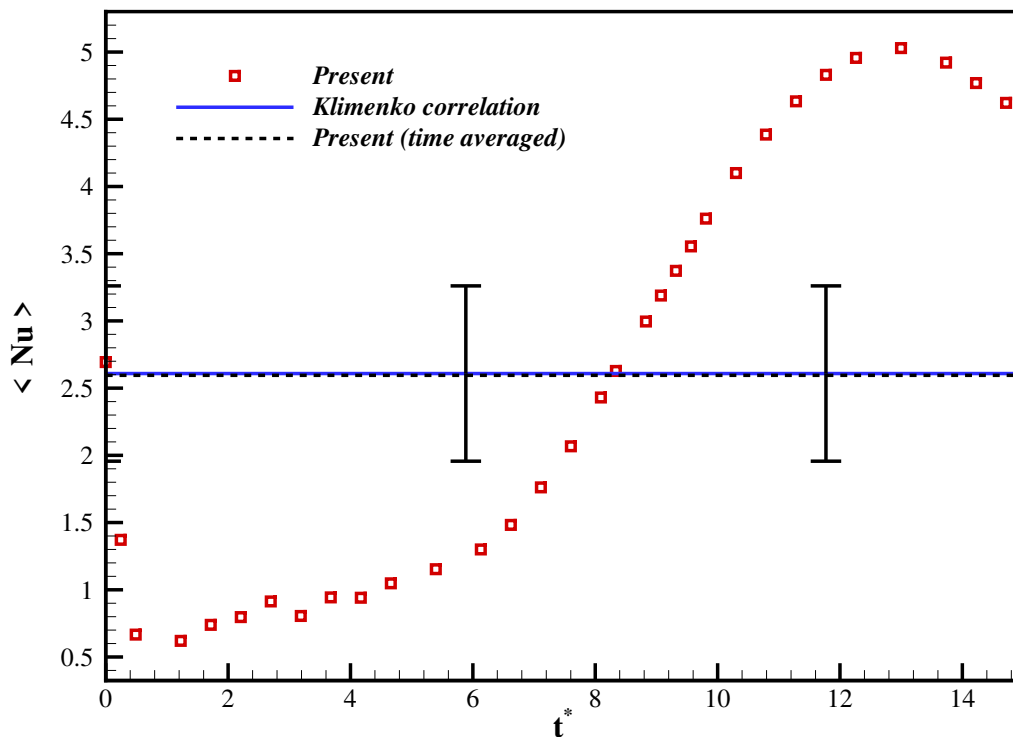


**Figure 7.** Space-averaged Nusselt number as a function of dimensionless time for  $Gr = 2482.58$ ,  $Ja = 0.064$  and  $Pr = 0.094$ . The error bars amount to  $\pm 25\%$  acceptable error as shown by Klimenko [53].

refer to the upstream (pre-shock) and downstream (post-shock) states, respectively. It has been shown that the necessary condition for stability of a shock wave is [19,56]:

$$-1 < h_D < 1 + 2M_1, \quad (120)$$

where  $0 < M_1 < 1$  is the downstream Mach number, which is measured in the reference frame that is moving with the shock. Under this condition, linear perturbations imposed on the shock front will asymptotically decay in time as  $t^{-3/2}$  [56].

According to the theory, a planar shock wave is unconditionally stable when propagating through an ideal-gas medium [57]. This can be easily evaluated, where  $h$  for an ideal gas EOS yields  $h_{D,ig} = -1/M_0^2$ , which always falls within the stability range (120). On the other hand, for non-ideal fluids, these stability conditions (120) can be violated, which leads to amplification of the perturbations until the structure of the flow field is altered [56]. It has been shown that the violation of the upper limit of the stability condition (120) corresponds to the splitting of the shock-front into two counter-propagating waves [58], while the violation of the lower limit is associated with the splitting of the shock front into two waves, travelling in the same direction [59].

Extensive theoretical investigations have been carried out to study the dynamics of the isolated planar shock waves propagating in an inviscid fluid medium. Namely, Bates [19,60] has derived analytical expressions for the amplitude of the ripples on the shock front, for initial sinusoidal perturbations.

According to Ref. [60], two families of solutions emerge depending on the sign of the following non-dimensional parameter:

$$\Lambda = \alpha^4 - 4\beta\Gamma\alpha^2 + 4\Gamma^2, \quad (121)$$

where

$$\alpha^2 = \frac{1 - M_1^2}{M_1^2}, \quad \beta = \frac{1 - h_{D1}}{2M_1}, \quad \Gamma = \frac{(1 + h_D)\eta}{2M_1} \quad (122)$$

are non-dimensional parameters as a function of downstream conditions and  $\eta = \rho_1/\rho_0$  is the compression ratio through the shock. For the case  $\Lambda > 0$ , the solution is given by:

$$\frac{\delta x(\tau)}{\delta x(0)} = \frac{2\alpha^2\sqrt{\beta^2 - 1}}{\sqrt{\Lambda}} \int_0^\infty (b \sin az \cos bz - a \cos az \sin bz) \frac{J_1(\alpha(\tau + z))}{\alpha(\tau + z)} dz, \quad (123)$$

where,  $\delta x$  is the amplitude of the ripple,  $\tau = Ukt/\eta$  is the non-dimensional time,  $U$  is the speed of the shock front in the laboratory reference of frame,  $k$  is the wave number of the initial ripple,  $J_1$  is the first-kind Bessel function and the parameters  $a$  and  $b$  are defined as:

$$a = \sqrt{\frac{2\beta\Gamma - \alpha^2}{4(\beta^2 - 1)} + \frac{\Gamma}{2(\beta^2 - 1)^{1/2}}}, \quad (124)$$

$$b = \sqrt{\frac{2\beta\Gamma - \alpha^2}{4(\beta^2 - 1)} - \frac{\Gamma}{2(\beta^2 - 1)^{1/2}}}, \quad (125)$$

and are real numbers. It is interesting to mention that the ideal-gas EOS belongs to this class of solutions. Using the asymptotic approximation  $J_1(x) \sim \sqrt{2}(\pi x)^{-1/2} \cos(x - 3\pi/4)$  as  $x \rightarrow \infty$  and considering Eq. (123), one can confirm that the amplitude of the ripple in a fluid medium with  $\Lambda > 0$  (such as an ideal gas) will decay in time with the negative power law  $\tau^{-3/2}$  in the long-time limit [60].

However, the situation can be different for fluids with an EoS that accept a negative  $\Lambda$ . Finally, for the case  $\Lambda < 0$ , the solution to the initial value problem is [60]:

$$\begin{aligned} \frac{\delta x(\tau)}{\delta x(0)} = & \frac{1}{2} \exp(-\sigma\tau) \cos a\tau - \left[ \frac{\Gamma}{\beta^2 - 1} - \frac{\alpha^2}{2(\beta^2 - 1)} \right] \frac{\exp(-\sigma\tau) \sin a\tau}{4a\sigma} \\ & + \frac{\alpha^2}{4\sigma\sqrt{\beta^2 - 1}} \left\{ \int_0^\tau \exp(-\sigma(\tau - z)) \left( \cos a(\tau - z) + \frac{\sigma}{a} \sin a(\tau - z) \right) \frac{J_1(\alpha z)}{\alpha z} dz \right. \\ & \left. + \int_0^\infty \left( \cos az + \frac{\sigma}{a} \sin az \right) \frac{J_1(\alpha(\tau + z))}{\alpha(\tau + z)} dz \right\}, \quad (126) \end{aligned}$$

where,  $\sigma = -ib$  is a real number. The presence of the exponential function implies a stronger damping compared to Eq. (123). However, the long time asymptotic is still a function of  $\tau^{-3/2}$  in both cases [60].

These theoretical considerations give us the opportunity to test and validate our numerical model also in the high-speed regime for the exotic shock-wave behavior of non-ideal gases. Our simulations consist of a long channel with periodic boundary conditions in the vertical direction. In all cases, the conductivity is set to zero and the viscosity is chosen to take the lowest possible value as long as the simulations are stable. In order to capture the shocks and avoid oscillations at the shock front, a third-order WENO scheme based on a 4-point stencil has been used in the reconstruction process instead of the third-order

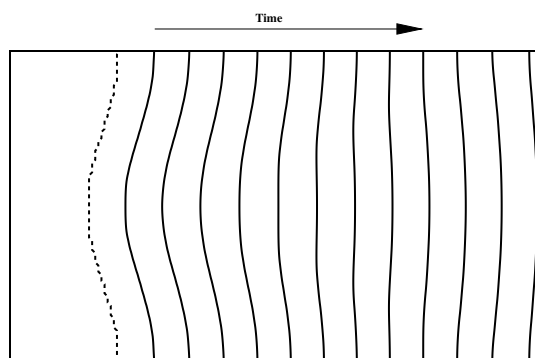


**Figure 8.** Evolution of an initially perturbed shock (dashed line) in time in an ideal gas medium with  $\gamma = 5/3$  and  $Ma = 3.0$ .

Lagrange polynomials as used in all other simulations. Three different cases have been selected; ideal-gas (IG) with  $M_0 = 3$ , vdW fluid with  $M_0 = 3.033$  and  $M_0 = 1.114$ . All other parameters are provided in table 1. In all cases, the shock front is initially perturbed with a single-mode sinusoidal function. The ratio of the amplitude to the wave length of the perturbation is 10%. The first two cases fall into the category of stable shocks, where the perturbations on the shock front are expected to decay in time. However, the last case is an example of shock-splitting, which will be discussed below. We now limit our focus on the first two cases. At time  $t = 0$ , the shock starts to propagate while it oscillates as it moves further towards the low-pressure side. We then measure the oscillation amplitude and compare it to the analytical expressions.

**Table 1.** Parameters for different cases of the simulation of the shock-stability

Case	EOS	$M_0$	$\rho_0$	$p_0$	$\nu$	$\delta t$	$C_v/R$	$h_D$	$\Lambda$
(1)	IG	3.0	1	1	$10^{-3}$	0.03	1.5	-1/9	4.214
(2)	vdW	3.033	$\rho_{cr}/3$	$0.66p_{cr}$	$10^{-4}$	0.1	3.0	-0.094	-7.856
(3)	vdW	1.114	$\rho_{cr}/3$	$0.66p_{cr}$	$10^{-6}$	0.4	80.0	-0.542	1.487

The initial shape of the shock front and its evolution in time is shown in Fig. 8 for the first case, where the oscillation of the front and the damping effect is apparent. Figure 9 shows the bird-eye view of this simulation.

According to the sign of  $\Lambda$ , the magnitude of the ripple for case (1) and case (2) were compared with analytical solutions (123) and (126), respectively. The results are presented in Fig. (10) and are in good agreement with the theory. It is apparent that our model captured the two distinct damping effects accurately, with more pronounced damping for the non-ideal fluid, as expected.

We now consider the exotic case (3). As mentioned earlier, non-ideal fluids can show exotic behaviors under certain conditions. Regarding case (3), due to its large specific heat value, the Hugoniot curve passes through regions, where the relation  $h_D < -1$  is satisfied. As argued in [14], this, together with the fact that the Hugoniot curve has more than two intersection points with the Rayleigh line (see Fig. 11), can cause the shock front to split into two traveling waves. Figure 12 presents our simulation for this case, where it is visible that the initial perturbation on the shock front has become unstable leading to splitting of the shock. The resulting waves, travel in the same direction with different speeds, as expected. This validates our model also for high-speed flows and shock-waves in real-gas media.

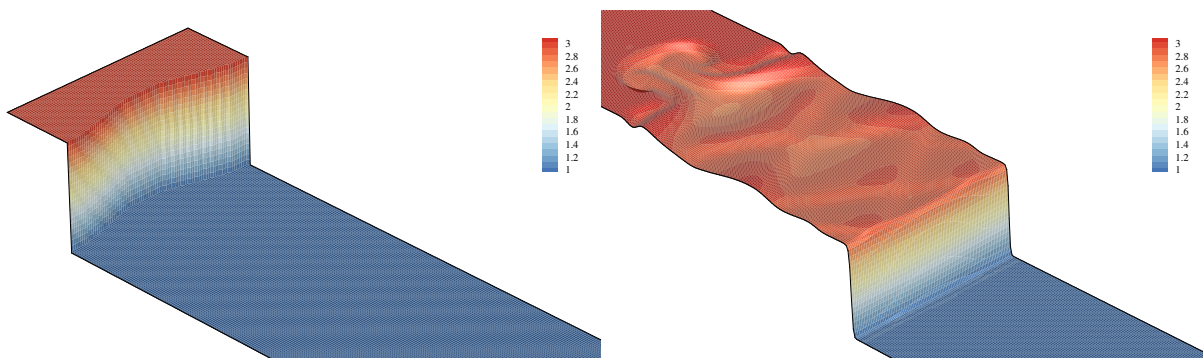


**Figure 9.** Case(1): left: Initial perturbation on the shock front. Right: evolution of the shock-front at time  $\tau = 9.73$ . Both plots and their coloring, show reduced density with respect to the pre-shock value  $\rho/\rho_0$ .

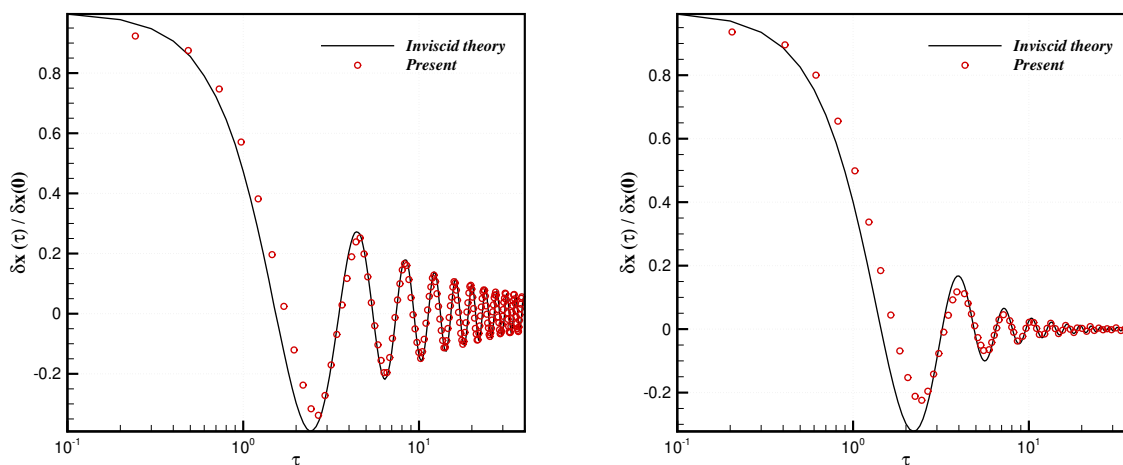


**Figure 10.** Comparison between the theoretical solution and the simulations for the ripple amplitude of an initially perturbed shock propagating through (left) an ideal gas with  $M_0 = 3.0$  (right) a vdW fluid with  $M_0 = 3.033$ .

#### 4. Conclusion

In this paper, we have presented a thorough study of our recently proposed model for compressible non-ideal flows. The model features full Galilean-invariance and the full energy equation is recovered for a non-ideal fluid, accounting also for two-phase systems and the presence of interfaces. It has been shown that the model is able to handle flows which are far into supercritical states. The effect of the inversion line on the  $T - P$  diagram was correctly captured for a vdW fluid in a wide range of reduced-pressure; from  $p_r = 3$  to  $p_r = 15$ . In addition, owing to the full energy conservation, the latent heat is already included in the model. This was shown on two different phase-change benchmarks: The one-dimensional Stefan problem and Boiling. As one of the advantages of the model, we were able to choose relatively large Stefan and Jacob numbers, which are scarce in the literature. Finally, the stability of an initially perturbed shock front in ideal gas and vdW fluid mediums with the Mach number  $Ma \approx 3$  were studied and compared to theoretical predictions. It was observed that the damping effect is much stronger in a vdW fluid as predicted by the inviscid theory. Beside from the fact that all of these simulations were implemented by taking only 9 discrete velocities, the results show that the real-gas effects have been properly captured by

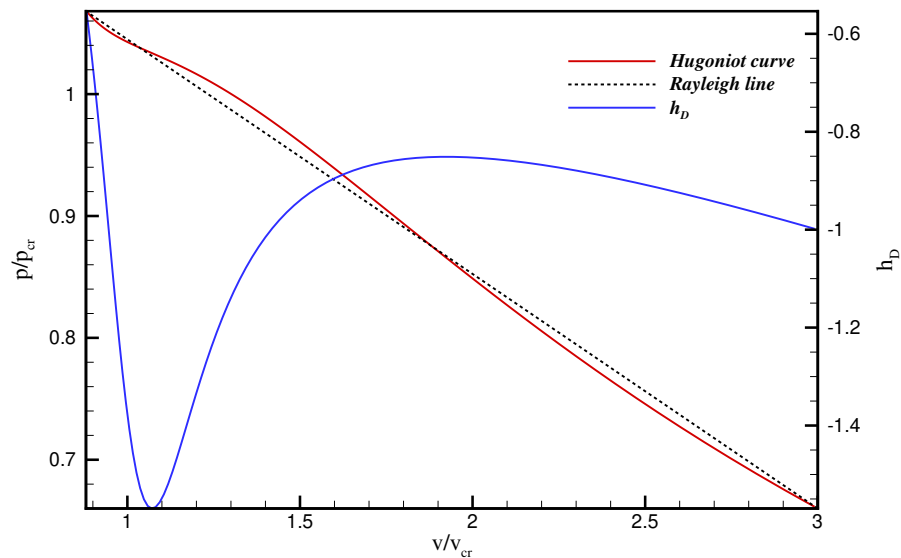


**Figure 11.** Case(3): The plot of  $h_D$  and the Hugoniot curve as a function of the downstream specific volume. It is visible that the Hugoniot curve has more than two intersection points with the Rayleigh line. Also, as the volume decreases, there are regions where  $h_D < -1$ .

the proposed model.

**Author Contributions:** E.R., B.D. and I.K. conceptualized the model. E.R. and B.D. developed the code. E.R. ran the simulations and validated the results. I.K. supervised the project. All authors contributed to writing the paper.

**Funding:** This work was supported by the European Research Council (ERC) Advanced Grant No. 834763-PonD and the Swiss National Science Foundation (SNSF) Grant No. 200021-172640. Computational resources at the Swiss National Super Computing Center (CSCS) were provided under Grant No. s897.

**Acknowledgments:** The authors would like to thank Prof. Jason Bates who provided useful information regarding his studies on shock stability analysis.

**Conflicts of Interest:** The authors declare no conflict of interest.

## Abbreviations

The following abbreviations are used in this manuscript:

LBM	Lattice Boltzmann method
RF	Reference frame
PonD	Particles on Demand

## References

1. Atif, M.; Kolluru, P.K.; Thantapanally, C.; Ansumali, S. Essentially Entropic Lattice Boltzmann Model. *Phys. Rev. Lett.* **2017**, *119*, 240602. doi:10.1103/PhysRevLett.119.240602.
2. Dorschner, B.; Bösch, F.; Chikatamarla, S.S.; Boulouchos, K.; Karlin, I.V. Entropic multi-relaxation time lattice Boltzmann model for complex flows. *Journal of Fluid Mechanics* **2016**, *801*, 623–651.

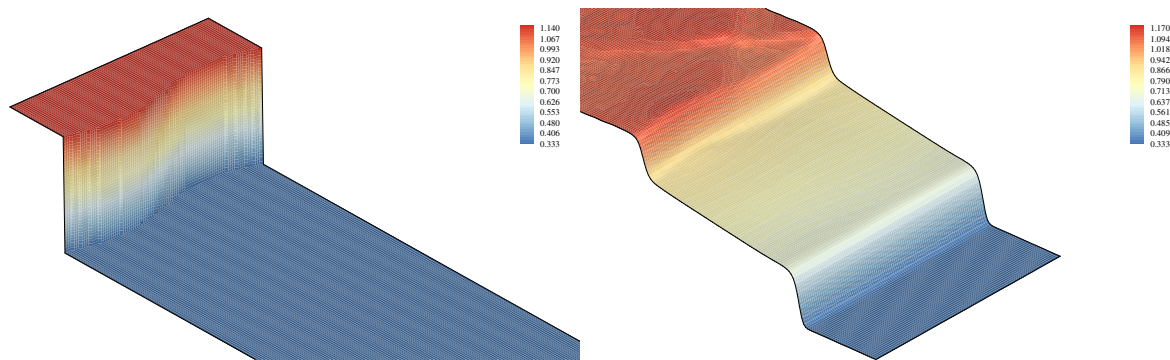


**Figure 12.** Case(3): left: initial perturbation on the shock front. Right: Evolution of the shock-front at time  $\tau = 16.3$ . The shock wave has split into two traveling waves in the same direction. Both plots and their coloring show reduced density with respect to the critical value  $\rho/\rho_{cr}$ .

3. Kunert, C.; Harting, J. Roughness Induced Boundary Slip in Microchannel Flows. *Phys. Rev. Lett.* **2007**, *99*, 176001. doi:10.1103/PhysRevLett.99.176001.
4. Hyvälouma, J.; Harting, J. Slip Flow Over Structured Surfaces with Entrapped Microbubbles. *Phys. Rev. Lett.* **2008**, *100*, 246001. doi:10.1103/PhysRevLett.100.246001.
5. Sbragaglia, M.; Benzi, R.; Biferale, L.; Succi, S.; Toschi, F. Surface Roughness-Hydrophobicity Coupling in Microchannel and Nanochannel Flows. *Phys. Rev. Lett.* **2006**, *97*, 204503. doi:10.1103/PhysRevLett.97.204503.
6. Biferale, L.; Perlekar, P.; Sbragaglia, M.; Toschi, F. Convection in Multiphase Fluid Flows Using Lattice Boltzmann Methods. *Phys. Rev. Lett.* **2012**, *108*, 104502. doi:10.1103/PhysRevLett.108.104502.
7. Benzi, R.; Chibbaro, S.; Succi, S. Mesoscopic Lattice Boltzmann Modeling of Flowing Soft Systems. *Phys. Rev. Lett.* **2009**, *102*, 026002. doi:10.1103/PhysRevLett.102.026002.
8. Mazloomi M, A.; Chikatamarla, S.S.; Karlin, I.V. Entropic Lattice Boltzmann Method for Multiphase Flows. *Phys. Rev. Lett.* **2015**, *114*, 174502. doi:10.1103/PhysRevLett.114.174502.
9. Succi, S. *The lattice Boltzmann equation: for fluid dynamics and beyond*; Oxford university press, 2001.
10. Qian, Y.H.; d’Humières, D.; Lallemand, P. Lattice BGK models for Navier-Stokes equation. *EPL (Europhysics Letters)* **1992**, *17*, 479.
11. Chen, H.; Chen, S.; Matthaeus, W.H. Recovery of the Navier-Stokes equations using a lattice-gas Boltzmann method. *Physical review A* **1992**, *45*, R5339.
12. Benzi, R.; Succi, S.; Vergassola, M. The lattice Boltzmann equation: theory and applications. *Physics Reports* **1992**, *222*, 145–197.
13. Chen, S.; Doolen, G.D. Lattice Boltzmann method for fluid flows. *Annual review of fluid mechanics* **1998**, *30*, 329–364.
14. Bates, J.W.; Montgomery, D.C. Some numerical studies of exotic shock wave behavior. *Physics of Fluids* **1999**, *11*, 462–475.
15. Zhao, N.; Mentrelli, A.; Ruggeri, T.; Sugiyama, M. Admissible shock waves and shock-induced phase transitions in a van der Waals fluid. *Physics of fluids* **2011**, *23*, 086101.
16. Guardone, A.; Vigeveno, L. Roe linearization for the van der Waals gas. *Journal of Computational Physics* **2002**, *175*, 50–78.
17. Zamfirescu, C.; Guardone, A.; Colonna, P. Admissibility region for rarefaction shock waves in dense gases. *Journal of Fluid Mechanics* **2008**, *599*, 363–381.
18. Bates, J.W.; Montgomery, D.C. The D’yakov-Kontorovich instability of shock waves in real gases. *Physical Review Letters* **2000**, *84*, 1180.
19. Bates, J.W. Instability of isolated planar shock waves. *Physics of Fluids* **2007**, *19*, 094102.
20. Swift, M.R.; Osborn, W.; Yeomans, J. Lattice Boltzmann simulation of nonideal fluids. *Physical review letters* **1995**, *75*, 830.

21. Holdych, D.; Rovas, D.; Georgiadis, J.G.; Buckius, R. An improved hydrodynamics formulation for multiphase flow lattice-Boltzmann models. *International Journal of Modern Physics C* **1998**, *9*, 1393–1404.
22. Guo, Z.; Zheng, C.; Shi, B. Discrete lattice effects on the forcing term in the lattice Boltzmann method. *Physical Review E* **2002**, *65*, 046308.
23. Huang, H.; Krafczyk, M.; Lu, X. Forcing term in single-phase and Shan-Chen-type multiphase lattice Boltzmann models. *Physical Review E* **2011**, *84*, 046710.
24. Lycett-Brown, D.; Luo, K.H. Improved forcing scheme in pseudopotential lattice Boltzmann methods for multiphase flow at arbitrarily high density ratios. *Physical Review E* **2015**, *91*, 023305.
25. Wagner, A.; Li, Q. Investigation of Galilean invariance of multi-phase lattice Boltzmann methods. *Physica A: Statistical Mechanics and its Applications* **2006**, *362*, 105–110.
26. He, X.; Doolen, G.D. Thermodynamic foundations of kinetic theory and lattice Boltzmann models for multiphase flows. *Journal of Statistical Physics* **2002**, *107*, 309–328.
27. Moqaddam, A.M.; Chikatamarla, S.S.; Karlin, I.V. Simulation of droplets collisions using two-phase entropic lattice Boltzmann method. *Journal of statistical physics* **2015**, *161*, 1420–1433.
28. Bösch, F.; Dorschner, B.; Karlin, I. Entropic multi-relaxation free-energy lattice Boltzmann model for two-phase flows. *EPL (Europhysics Letters)* **2018**, *122*, 14002.
29. Moqaddam, A.M.; Chikatamarla, S.S.; Karlin, I.V. Drops bouncing off macro-textured superhydrophobic surfaces. *Journal of Fluid Mechanics* **2017**, *824*, 866–885.
30. Dorschner, B.; Chikatamarla, S.S.; Karlin, I.V. Fluid-structure interaction with the entropic lattice Boltzmann method. *Physical Review E* **2018**, *97*, 023305.
31. Zhang, R.; Chen, H. Lattice Boltzmann method for simulations of liquid-vapor thermal flows. *Physical Review E* **2003**, *67*, 066711.
32. Kamali, M.; Gillissen, J.; Van den Akker, H.; Sundaresan, S. Lattice-Boltzmann-based two-phase thermal model for simulating phase change. *Physical Review E* **2013**, *88*, 033302.
33. Kupershtokh, A.L.; Medvedev, D.A.; Griбанov, I.I. Thermal lattice Boltzmann method for multiphase flows. *Physical Review E* **2018**, *98*, 023308.
34. Reyhanian, E.; Dorschner, B.; Karlin, I.V. Thermokinetic lattice Boltzmann model of nonideal fluids. *Physical Review E* **2020**, *102*, 020103.
35. Dorschner, B.; Bösch, F.; Karlin, I.V. Particles on Demand for Kinetic Theory. *Phys. Rev. Lett.* **2018**, *121*, 130602. doi:10.1103/PhysRevLett.121.130602.
36. Krämer, A.; Küllmer, K.; Reith, D.; Joppich, W.; Foysi, H. Semi-Lagrangian off-lattice Boltzmann method for weakly compressible flows. *Physical Review E* **2017**, *95*, 023305.
37. Di Ilio, G.; Dorschner, B.; Bella, G.; Succi, S.; Karlin, I.V. Simulation of turbulent flows with the entropic multirelaxation time lattice Boltzmann method on body-fitted meshes. *Journal of Fluid Mechanics* **2018**, *849*, 35–56.
38. Shan, X.; He, X. Discretization of the velocity space in the solution of the Boltzmann equation. *Physical Review Letters* **1998**, *80*, 65.
39. Ansumali, S.; Karlin, I.V. Kinetic boundary conditions in the lattice Boltzmann method. *Physical Review E* **2002**, *66*, 026311.
40. Grad, H. On the kinetic theory of rarefied gases. *Communications on pure and applied mathematics* **1949**, *2*, 331–407.
41. Karlin, I.; Sichau, D.; Chikatamarla, S. Consistent two-population lattice Boltzmann model for thermal flows. *Physical Review E* **2013**, *88*, 063310.
42. Kupershtokh, A.; Medvedev, D.; Karpov, D. On equations of state in a lattice Boltzmann method. *Computers & Mathematics with Applications* **2009**, *58*, 965–974.
43. Liu, J. Thermal Convection in the van der Waals Fluid. In *Frontiers in Computational Fluid-Structure Interaction and Flow Simulation*; Springer, 2018; pp. 377–398.
44. Li, Q.; Zhou, P.; Yan, H. Revised Chapman-Enskog analysis for a class of forcing schemes in the lattice Boltzmann method. *Physical Review E* **2016**, *94*, 043313.

45. Lycett-Brown, D.; Luo, K.H. Multiphase cascaded lattice Boltzmann method. *Computers & Mathematics with Applications* **2014**, *67*, 350–362.
46. Wagner, A. Thermodynamic consistency of liquid-gas lattice Boltzmann simulations. *Physical Review E* **2006**, *74*, 056703.
47. Welch, S.W.; Wilson, J. A volume of fluid based method for fluid flows with phase change. *Journal of computational physics* **2000**, *160*, 662–682.
48. Onuki, A. Dynamic van der Waals theory of two-phase fluids in heat flow. *Physical review letters* **2005**, *94*, 054501.
49. Onuki, A. Dynamic van der Waals theory. *Physical Review E* **2007**, *75*, 036304.
50. Zuber, N. Nucleate boiling. The region of isolated bubbles and the similarity with natural convection. *International Journal of Heat and Mass Transfer* **1963**, *6*, 53–78.
51. Kocamustafaogullari, G. Pressure dependence of bubble departure diameter for water. *International communications in heat and mass transfer* **1983**, *10*, 501–509.
52. Esmaeeli, A.; Tryggvason, G. Computations of film boiling. Part I: numerical method. *International journal of heat and mass transfer* **2004**, *47*, 5451–5461.
53. Klimenko, V.; Shelepen, A. Film boiling on a horizontal plate—a supplementary communication. *International Journal of Heat and Mass Transfer* **1982**, *25*, 1611–1613.
54. D'yakov, S. Shock wave stability. *Zh. Eksp. Teor. Fiz* **1954**, *27*, 288–295.
55. Kontorovich, V. Concerning the stability of shock waves. *Soviet Phys. JETP* **1958**, *6*.
56. Bates, J. On the theory of a shock wave driven by a corrugated piston in a non-ideal fluid. *Journal of fluid mechanics* **2012**, *691*, 146–164.
57. Landau, L.D.; Lifshitz, E.M. Fluid mechanics 2nd ed. *Pergamon* **1987**, pp. 61–252.
58. Gardner, C. Comment on “Stability of Step Shocks”. *Physics of Fluids (New York)* **1963**, *6*.
59. Bethe, H. The theory of shock waves for an arbitrary equation of state. Technical paper 545, Office Sci. Res. & Dev **1942**.
60. Bates, J.W. Initial-value-problem solution for isolated rippled shock fronts in arbitrary fluid media. *Physical Review E* **2004**, *69*, 056313.